RSC Applied Polymers

ROYAL SOCIETY OF CHEMISTRY

PAPER

View Article Online
View Journal | View Issue

Cite this: *RSC Appl. Polym.*, 2023, **1**, 111

Experimental and computational studies on the effects of C(2) methylation on the properties and gas separation performance of polyimide-ionene membranes†

Grayson P. Dennis, [a] Kathryn E. O'Harra, [a] Xiaoyang Liu, [a] Enrique M. Jackson,[b] C. Heath Turner [a] and Jason E. Bara [a]*

As methylation of the imidazolium C(2) position is known to affect the intermolecular properties of ionic liquids (ILs), polyimide (PI)-ionenes were designed to determine what effects the presence of a C(2)–Me group might have on the properties and membrane performance characteristics relative to analogous PI-ionenes with a C(2)–H group. A commonly used IL (1-butyl-3-methylimidazolium bistriflimide, $[C_4mim][Tf_2N]$) was added to the synthesized polymers which formed homogeneous PI-ionene + IL composites that were amenable to the formation of flexible films suitable for membrane testing. The gas permeation behaviors of the resultant membranes were measured for H_2, CO_2, N_2, and CH_4. The 6FDA-containing PI-ionene exhibited greater gas permeabilities than the PMDA-containing material, while both materials exhibited comparable selectivity for CO_2 relative to other gases. The permeability–selectivity relationships were visualized on Robeson plots, and these PI-ionene membranes were comparable to other ionene and poly(IL) materials. Molecular dynamics (MD) simulations and quantum mechanics (QM) calculations were performed on the C(2)–H and C(2)–Me monomeric units to determine their conformations and other structural properties. The results obtained are useful in the further development of ionene polymers for gas separation membranes.

Received 21st June 2023,
Accepted 29th August 2023

DOI: 10.1039/d3lp00092c

rsc.li/rscapplpolym

1. Introduction

Although multiple types of processes exist to separate CO_2 from various industrial gas streams, membranes offer inherent advantages of pressure-driven, solution–diffusion (S–D) transport of solutes through dense polymer materials. In the S–D mechanism, separation of gases through polymer membranes is influenced by the available free volume through which diffusion can occur for a given gas (and its relative size) and the thermodynamics of gas-polymer interactions which govern solubility – essentially the product of "*how much*" (*i.e.*, S) and "*how fast*" (*i.e.*, D). The S and D properties of polymer gas separation membranes can be controlled/tailored *via* molecular design.

Among the many different polymer types that have been studied as gas separation membranes, polyimides (PIs) exhibit CO_2 selectivity in addition to robust thermal and mechanical properties. PIs are condensation polymers formed through the reaction of a dianhydride and diamine (*i.e.*, ring closure with loss of water molecule). Common dianhydrides used in polyimide synthesis include pyromellitic dianhydride (PMDA), 4,4′-(hexafluoroisopropylidene)diphthalic anhydride (6FDA), and 3,3′,4,4′-benzophenonetetracarboxylic dianhydride (BTDA) (Fig. 1). Examples of common diamines used in polyimide synthesis such as 4,4′-oxydianiline (ODA), *p*-phenylenediamine (PPD), and 4,4′-methylenedianiline (MDA) are also shown in Fig. 1.

Combinations of these dianhydrides and diamines are used to form polymers with excellent chemical, thermal, and

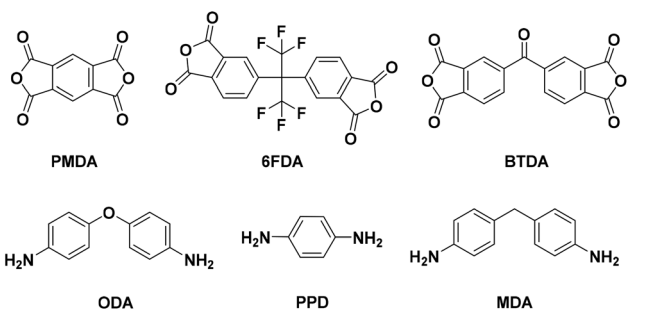

Fig. 1 Common dianhydrides (top) and diamines (bottom) used in commercial PI materials.

[a]*University of Alabama, Department of Chemical & Biological Engineering, Tuscaloosa, AL 35487-0203, USA. E-mail: Jbara@eng.ua.edu*
[b]*NASA Marshall Space Flight Center, Huntsville, AL 35812, USA*

† Electronic supplementary information (ESI) available. See DOI: https://doi.org/10.1039/d3lp00092c

mechanical properties – traits which are required for viable membrane formation. Kapton® (Fig. 2) is a well-known commercial PI formed *via* condensation polymerization between PMDA and ODA.

O'Brien *et al.* measured the CO_2 permeability (P_{CO_2}) of a commercial sample of Kapton H® to be 0.22 barrer, yet a polymer with an identical backbone synthesized in their work from PMDA + ODA was measured as P_{CO_2} = 2.71 barrer. This ~12× increase was attributed to the processing method(s) which influenced the aggregation and chain orientations within the film.[1]

One of the main conclusions of a review by Hirayama and co-workers on the structure–property relationship of PIs was that the addition of methyl groups to the PI backbone increases P_{CO_2}.[2] The presence of pendant groups on polymer backbones can have significant effects on the performances of gas separation membranes. Stern, *et al.* showed that the selection of diamine, which varied only with the presence of a methyl group, greatly affected the PI microstructure and gas permeation behaviors.[3] When a methyl group was added onto the CH_2CH_2 bridge of 4,4′-(ethane-1,2-diylbis(oxy))dianiline (Fig. 3) and reacted with 6FDA to form PIs, the CO_2/CH_4 permselectivities increased by over 50% while P_{CO_2} decreased by 30%.[3]

Hirayama and co-workers did an extensive test of over 43 PI homopolymers formed from various combinations of dianhydrides and diamines.[2] Comparing two PI materials formed using 6FDA, 3,3′-dimethyl-4,4′-diaminodiphenylmethane (Fig. 4a), and 3,3′,5,5′-tetramethyl-4,4′-diaminodiphenylmethane (Fig. 4b), the results show that the addition of methyl groups drastically changed the sterics and thus the permeabilities of the resultant materials. The addition of two more methyl groups onto a phenylene diamine caused the resulting 6FDA-containing PI to increase in P_{CO_2} by 500% while only decreasing the CO_2/CH_4 permselectivity by 33%.[2] Depending on the position and bulk of R group(s), the final properties of materials with similar backbones can be markedly different.

Ionenes are a broad class of polymers which contain ionic groups (*e.g.*, ammonium, imidazolium, phosphonium, *etc.*) directly within the polymer backbone.[4–8] Historically, the vast majority of ionenes in the literature have contained ammonium cations tethered by simple alkyl linkages.[9,10] However, in recent years, imidazolium ionenes are becoming of greater interest due to tremendous growth in the study of ionic liquids (ILs), particularly in membrane-based separation of CO_2 from various gas streams.[11,12] The numerous synthetic strategies available for imidazolium ionenes present opportunities to create highly tailored charged polymers that also contain structural elements found in the aforementioned PIs. Due to their "hybrid" characteristics, the design of imidazolium PI-ionenes and composites with ILs present unique possibilities in the design of polymer gas separation membranes.

One example of a PI-ionene was presented by Li,[13] where 6FDA-containing random or block copolymers containing imidazolium moieties and MDA (see Fig. 1) demonstrated good CO_2 selectivities. Although the P_{CO_2} decreased with increasing ionic content, the CO_2/CH_4 selectivity increased; however, it should be noted that the number average molecular weight (M_N) of both random and block copolymers were considerably lower as the fraction of the ionic components increased, indicating potential synthetic challenges when starting from imidazolium-containing diamines.[13–15]

Rather than form PI-ionenes directly through reaction of an imidazolium-containing diamine with a dianhydride, our group has found that higher molecular weights are achieved by first forming a bis(imidazole) diimide that is then polymerized with an α,ω-dihalide (or similar compound) *via* the Menshutkin reaction (forming the imidazolium group upon polymerization), followed by anion-exchange from a halide to a molecular anion. Mittenthal *et al.*, demonstrated this concept forming a PMDA-containing PI-ionene (Fig. 5) which showed excellent film forming qualities.[16]

Although the neat PI-ionene in Fig. 5 had a P_{CO_2} of ~1 barrer, soaking the film in 1-butyl-3-methylimidazolium bistriflimide ([C_4mim][Tf_2N]) IL (which was absorbed at ~1 eq. by the polymer) increased P_{CO_2} by more than 2000%.[16] Multiple works from our group have since expanded on the concept of

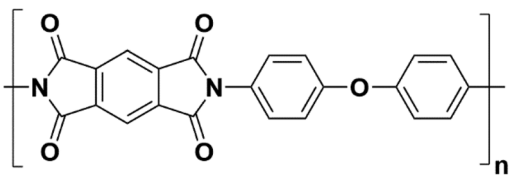

Fig. 2 Structure of Kapton®.

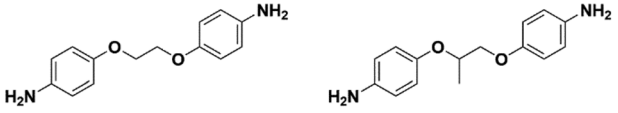

Fig. 3 Structures of 4,4′-(ethane-1,2-diylbis(oxy))dianiline (left) and 4,4′-(propane-1,2-diylbis(oxy))dianiline (right).

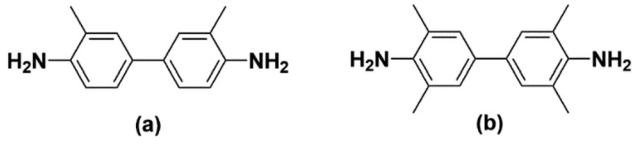

Fig. 4 Methylated biphenyl diamine monomers used by Hirayama *et al.* where (a) is 3,3′-dimethyl-4,4′-diaminodiphenylmethane and (b) is 3,3′,5,5′-tetramethyl-4,4′-diaminodiphenylmethane.

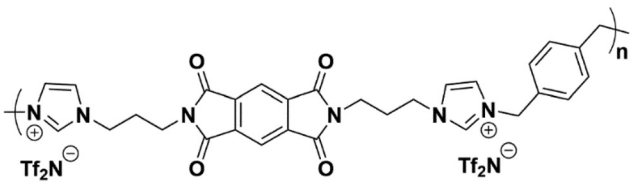

Fig. 5 PMDA-containing PI-ionene reported by Mittenthal *et al.*[16]

PI-ionenes built from PMDA or 6FDA, demonstrating that these synthetic methods can be applied to provide great control over the backbone structure, while achieving molecular weights >100 kDa that are favorable for formation of mechanically stable, thin films. Furthermore, each of these PI-ionenes also exhibits favorable interactions with ILs to form composites with ILs with enhanced P_{CO_2} relative to the neat PI-ionenes.[17,18]

Although our group has examined multiple structural variations within PI-ionenes and related polymers, the effects of methyl groups present on the imidazolium ring has not yet been explored. Within the study of IL properties, there has been a strong focus on understanding the effects of methylation of the imidazolium C(2) position of the imidazolium ring.[19–24] The C(2)–H is considered to be "acidic" and able to experience H-bonding with anions, and this behavior is attributed as a differentiating factor between low melting imidazolium salts and other organic salts (*e.g.*, quaternary ammonium). "Blocking" this H-bonding *via* introduction of a methyl (or other) group at the C(2) position is usually correlated with increases in IL viscosity and melting point compared to analogous ILs with a C(2)–H, with a benefit of increased stability to alkaline media.[25] However, the effects of this methylation on CO_2 solubility are not as obvious. These changes indicate that the interactions in imidazolium ILs with C(2)–Me groups are distinctly different than those with C(2)–H groups. Although the exact nature of these interactions are still under debate, Fumino *et al.* confirms the methylation of the imidazolium C(2) position causes the H-bonding effect to transition toward coulombic interactions between the ions.[26]

Carlisle, Bara, and co-workers have shown that relatively simple imidazolium ionenes can be formed in two steps *via* the reaction of 2-methylimidazole and 1,10-dibromodecane (Fig. 6).[27]

To the best of our knowledge, the alkyl-linked imidazolium ionene depicted in Fig. 6 is the only instance of an imidazolium ionene with an imidazolium C(2)–Me group in the literature.[27] Carlisle's imidazolium ionenes were amenable to casting into thin films *via* melt processing, whether as the Br^- or Tf_2N^- forms. However, gas permeabilities varied greatly with anion type, with P_{CO_2} = 0.13 barrer and 5.3 barrer, for the Br^- and Tf_2N^- forms, respectively.[27] Carlisle was unable to compare the ionene in Fig. 6 to a structurally analogous polymer without methylation (*i.e.*, C(2)–H) due to limitations of the synthetic method.

He *et al.* synthesized imidazolium oligomers of exact molecular weight using 2-methylimidazole.[28] These oligomers offered excellent synthetic control, allowing for differing anions to be coordinated with the C(2)–Me imidazolium

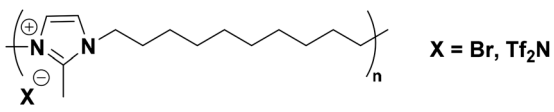

Fig. 6 "Main-chain imidazolium ionene" containing 2-methylimidazolium cations tethered by *n*-decyl chains.

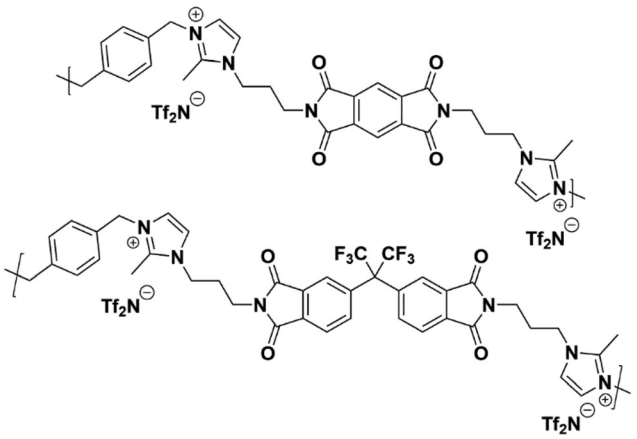

Fig. 7 Structures of [PMDA-2MeAPI(pXy)][Tf_2N] (top) and [6FDA-2MeAPI(pXy)][Tf_2N] (bottom).

cations. Even though these were used for peptide synthesis, this approach is notable as it is likely the first report of a unidirectional ionene synthesis.[28]

Thus, the effects of a C(2)–Me functional group on the properties of imidazolium ionenes and associated gas separation membranes remain unexplored. Herein, we explore these behaviors through two new PI-ionenes: [PMDA-2MeAPI(pXy)][Tf_2N] and [6FDA-2MeAPI(pXy)][Tf_2N] (Fig. 7), which were respectively synthesized by first reacting PMDA or 6FDA with 1-(3-aminopropyl)-2-methylimidazole (2-MeAPI), followed by polymerization *via* Menshutkin reaction with *para*-dichloroxylene and subsequent anion metathesis to the $[Tf_2N]^-$ form. To aid in the formation of thin films suitable for gas separation membranes, IL was directly added to the casting solution, and the non-volatile IL is held within the polymer film after solvent evaporation. The resulting materials were characterized and tested as gas separation membranes to begin developing an understanding as to how the presence of a methyl group at the C(2) position of the imidazolium cation affects the structure–property relationships in PI-ionenes. Furthermore, quantum mechanics (QM) and molecular dynamics (MD) simulations were performed on the PMDA-2MeAPI and 6FDA-2MeAPI monomers to gain further insight into the effects on the film's characteristics and gas separation ability.

2. Experimental section

2.1 Materials

PMDA (>99%) and 6FDA (>99%) were purchased from Akron Polymer Systems. *para*-dichloroxylene (*p*DCXy, >98%) was purchased from TCI. $LiTf_2N$ was purchased from 3M. *N*-Methylpyrrolidone (NMP, ACS grade), tetrahydrofuran (THF, ACS grade), diethyl ether (Et_2O, ACS grade), methanol (MeOH), ammonium hydroxide (NH_4OH, 28–30% in water, ACS Grade), and *N*,*N*-dimethylformamide (DMF, anhydrous), were purchased from VWR. RANEY® Nickel®2800 slurry in H_2O and

triethylamine (Et_3N) were purchased from Oakwood Chemical. 2-Methylimidazole was purchased from Alfa Aesar. Celite® 545 was purchased from Millipore-Sigma. Acrylonitrile (≥ 99%) was purchased from Sigma-Aldrich. All materials were used as obtained, without further purification. Deionized H_2O (DI H_2O, 12 MW) was obtained from the Department of Chemistry at The University of Alabama.

2.2 Synthesis of 3-(2-methyl-1*H*-imidazol-1-yl)propan-1-amine ("2MeAPI")

The synthesis of 2MeAPI has been detailed in our previous work[29] based on methods originally reported by Schwan for 1-(3-aminopropyl)imidazole.[30] The corresponding nitrile (*i.e.*, R-CN) precursor was prepared from 2-methylimidazole, acrylonitrile, and Et_3N in refluxing toluene, and was subsequently reduced to 2MeAPI (*i.e.*, R-NH_2) with H_2 in the presence of RANEY® nickel in MeOH/NH_4OH (aq).

2.3 Synthesis of 2MeAPI-diimide monomers

2.3.1 Synthesis of 2,6-bis(3-(2-methyl-1*H*-imidazol-1-yl)propyl) pyrrolo[3,4-*f*]isoindole-1,3,5,7(2*H*,6*H*)-tetraone ("PMDA-2MeAPI"). PMDA-2MeAPI was synthesized according to Scheme 1. PMDA (10.00 g, 45.8 mmol) and 2MeAPI (13.4 g, 96.3 mmol) were added with 80 mL DMF to a 250 mL heavy-walled pressure vessel (Ace Glass) sealed with a threaded PTFE cap with a DuPont Kalrez® O-ring. The sealed reaction vessel was heated at 120 °C for 24 h. The reaction was cooled and the contents were poured into DI H_2O and stirred at RT for 1 h. The precipitated solids were washed with 2 × 50 mL DI H_2O and dried in a vacuum oven at 100 °C overnight to yield an off-white powder (18.7 g, 89%).

^{1}H-NMR (500 MHz, d6-DMSO) δ 8.21 (s, 2H), 7.12 (s, 2H), 6.74 (s, 2H), 3.98 (t, J = 7.24 Hz, 4H), 3.66 (t, J = 6.10 Hz, 4H), 2.29 (s, 6H), 2.06 (p, J = 6.51, 6.71 Hz, 4H). ^{13}C-NMR (500 MHz, d6-DMSO) δ 166.85, 144.11, 137.48, 126.65, 119.88, 117.51, 43.37, 36.06, 29.12, 13.04.

2.3.2 Synthesis of 5,5′-(perfluoropropane-2,2-diyl)bis(2-(3-(2-methyl-1*H*-imidazol-1-yl)propyl) isoindoline-1,3-dione) ("6FDA-2MeAPI"). 6FDA-2MeAPI was synthesized according to Scheme 2 *via* the reaction of 6FDA and 2MeAPI. 6FDA (5.00 g, 11.3 mmol) was added to a 250 mL round bottom flask with 30 mL of DMF. The sealed reaction vessel was cooled to 5 °C and stirred for 1 h. 2MeAPI (3.45 g, 24.8 mmol) was then added to the flask, was removed from the cooling source and the vessel was allowed to warm to room temperature while stirring for 16 h. Toluene (15 mL) was then added and the flask equipped with a reflux condenser. The vessel was heated at 125 °C for 24 h. The solution was cooled, and toluene and some DMF were removed *via* rotary evaporation. The remaining solution was poured into 400 mL of DI H_2O to precipitate the product. The solids were filtered and washed with 2 × 100 mL of DI H_2O. The product was collected and dried for 24 h at 120 °C in a vacuum oven. The product was a tan powder (6.12 g, 82%).

^{1}H-NMR (500 MHz, d6-DMSO) δ 8.08 (d, J = 8.06 Hz, 2H), 7.88 (d, J = 7.99 Hz, 2H), 7.66 (s, 2H), 7.11(s, 2H), 6.73 (s, 2H), 3.97 (t, J = 7.11 Hz, 4H), 3.63 (t, J = 6.62 Hz, 4H), 2.29 (s, 6H), 2.03 (p, J = 6.76, 6.93 Hz, 4H). ^{13}C-NMR (500 MHz, d6-DMSO) δ167.55, 167.42, 144.18, 137.44, 135.99, 133.63, 133.22, 125.62, 124.34, 123.61, 120.15, 64.61, 43.55, 35.75, 29.09, 12.75.

2.4 Synthesis of PI-ionenes

2.4.1 Synthesis of [PMDA-2MeAPI(pXy)][Tf_2N]. PMDA-2MeAPI was polymerized with an equimolar equivalent of pDCXy to form a PI-ionene with a xylyl linkage *via* the Menshutkin reaction as shown in Scheme 3. PMDA-2MeAPI (5.00 g, 10.9 mmol) and pDCXy (1.90 g, 10.9 mmol) were added with 80 mL of NMP to a 250 mL round-bottom heavy-walled pressure vessel. The sealed reaction vessel was heated at 150 °C for 24 h. The solvent was decanted, and the gel precipitate was dissolved in warm DI H_2O. This polymer solution was solubilized as the Cl^- salt and, subsequently, poured into DI H_2O containing $LiTf_2N$ (2.5 eq., 7.8 g) to promote exchange of the anion. The ionene was vigorously stirred with an overhead mechanical mixer for 24 h at RT to ensure complete anion metathesis to the [Tf_2N^-] form. The product was then filtered and dried in a vacuum oven at 120 °C overnight.

To remove residual low molecular weight content, THF (100 mL) was added to [PMDA-2MeAPI(pXy)][Tf_2N] and the two-phase mixture stirred at RT for 4 h. The lower polymer layer separates as a viscous brown gel, and the upper THF layer containing solvent and oligomeric compounds was decanted. Finally, the polymer was reprecipitated in Et_2O and filtered. The ionene product was dried to yield a light tan glassy solid (9.42 g, 77%).

^{1}H NMR (500 MHz, DMSO) δ 8.24 (s, 2H), 7.74 (d, J = 15.8 Hz, 4H), 7.38 (s, 4H), 5.44 (s, 4H), 4.24 (s, 4H), 3.72 (s, 4H), 2.64 (s, 6H), 2.16 (s, 4H).

2.4.2 Synthesis of [6FDA-2MeAPI(pXy)][Tf_2N]. 6FDA-2MeAPI was polymerized with an equimolar equivalent of pDCXy according to the same procedure as the analogous PMDA-containing ionene as shown in Scheme 4. 6FDA-2MeAPI (5.00 g,

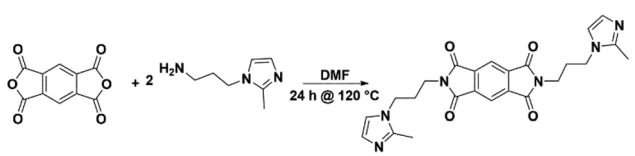

Scheme 1 Synthesis schematic of PMDA-2MeAPI monomer.

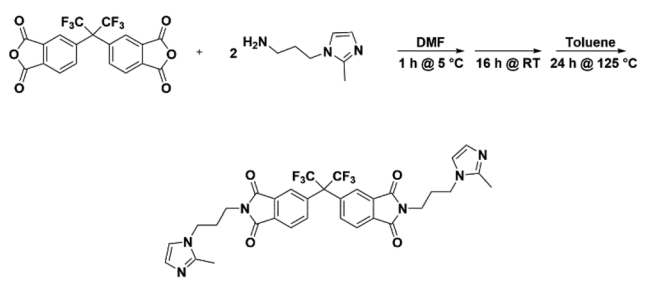

Scheme 2 Synthesis schematic of 6FDA-2MeAPI monomer.

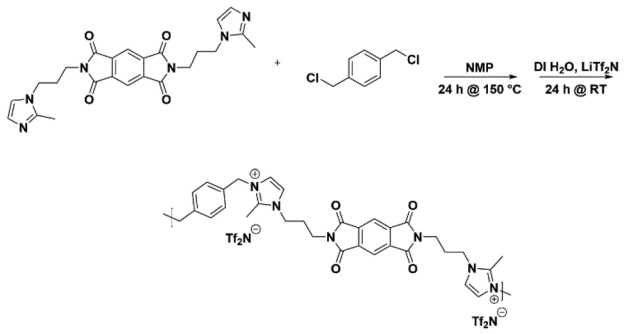

Scheme 3 Synthesis of [PMDA-2MeAPI(pXy)][Tf_2N].

7.28 mmol) and pDCXy (1.27 g, 7.28 mmol) were added with 50 mL of anhydrous DMF to a round-bottom heavy-walled pressure vessel, and the pressure vessel was sealed with a PTFE stopper and Kalrez® O-ring. The reaction was heated to 120 °C for 24 h. The solvent was decanted, and solids were dissolved in DI H_2O. This polymer solution was isolated as the Cl^- salt, and the solution was subsequently poured into DI H_2O containing $LiTf_2N$ (2.5 eq., 5.23 g) to promote anion exchange. The [6FDA-2MeAPI(pXy)][Tf_2N] ionene was stirred for 24 h at RT to ensure anion metathesis to the $[Tf_2N]^-$ form. The product was then filtered and dried in a vacuum oven at 120 °C overnight.

Low molecular weight content was removed using THF in an identical manner to that for the PMDA-containing PI-ionene. [6FDA-2MeAPI(pXy)][Tf_2N] was dried to yield a tan powder (7.57 g, 74%).

^{1}H NMR (500 MHz, DMSO) δ 8.09 (d, J = 8.1 Hz, 2H), 7.84 (s, 2H), 7.70 (s, 6H), 7.36 (s, 4H), 5.41 (s, 4H), 4.20 (s, 4H), 3.67 (s, 4H), 2.63 (s, 6H), 2.10 (d, J = 8.0 Hz, 4H).

2.5 Membrane preparation

The non-methylated PI-ionene counterparts were able to form films by solvent casting methods, without the use of IL. The membrane forming ability of the non-methylated counterparts demonstrated the essential nature of the C(2) position of the imidazolium cation. The addition of [C_4mim][Tf_2N] to these membranes allowed for thin, flexible membrane formation. Membranes were prepared by dissolving ~1 g of polymer in ~10 mL of acetone in a 20 mL scintillation vial. One molar equivalent of [C_4mim][Tf_2N] per polymer repeat unit was then added to each solution. Rain-X®, a hydrophobic coating, was buffed onto a 6″ × 6″ glass plate to aid in the eventual release of the polymer films from the glass surface. The solution was cast onto these glass plates and left overnight at ambient conditions. The resulting film was then placed into a vacuum oven at 80 °C for 24 h. These films peeled easily from the plates yet were slightly tacky, so the resulting films was placed onto highly permeable Supor® PES supports prior to insertion in the membrane systems. Although the membrane was supple, it remained as a thin (*i.e.*, 20–30 μm) layer selective later atop the Supor® substrate, which can be seen in the SEM images in the Fig. S12 and S13.†

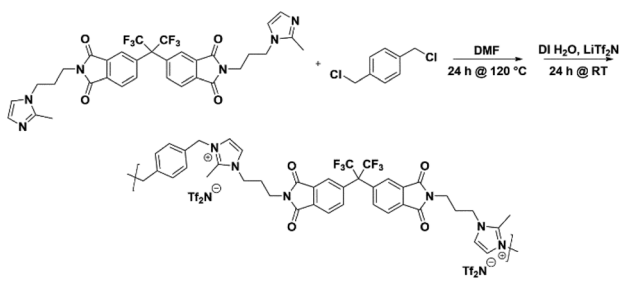

Scheme 4 Synthesis of [6FDA-2MeAPI(pXy)][Tf_2N].

2.6 Material characterization

^{1}H and ^{13}C NMR were used to characterize the monomers PMDA-2MeAPI and 6FDA-2MeAPI, and ^{1}H NMR for the polymers [PMDA-2MeAPI(pXy)][Tf_2N] and [6FDA-2MeAPI(pXy)][Tf_2N] using a Bruker Avance (360 MHz or 500 MHz for ^{1}H, 500 MHz for ^{13}C). ^{1}H- and ^{13}C-NMR spectra are presented in Fig. S1–S6.†

FT-IR spectroscopy was performed using a PerkinElmer Spectrum Two spectrometer with the UATR accessory. (Fig. S7†). The spectra were normalized at the carbonyl peak (C═O stretching vibrations at ~1720 cm^{-1}).

Matrix assisted laser deionization/ionization-time of flight (MALDI-TOF) mass spectroscopy was performed using a Bruker Ultraflex on both polymers to determine the mass of the most prominent peak or mode of the distribution (M_p), and thus alongside NMR end-group analysis provide excellent estimates of M_N. The graphs can be seen in Fig. S8.†

Wide-angle X-ray diffraction (WAXD) was carried out using a Bruker D8 Discover with GADDS using a cobalt source (K_α = 1.79 Å) with a point collimator. The detector was a Vantec 500 area detector. The domain spacing (*d*-spacing) was determined for each material along with their [C_4mim][Tf_2N] composite counterparts. The *d*-spacing was calculated using Bragg's law. The 2θ range for WAXD was 5 to 55°.

Differential scanning calorimetry (DSC) was performed using a TA instruments Q20. Each sample was cycled three times from 25 °C to 250 °C at a rate of 10 °C min^{-1} under N_2 atmosphere. Thermal gravimetric analysis (TGA) was carried out on a Seiko TG-DTA 7300. The samples were run starting at room temperature running up to 700 °C at a heating rate of 10 °C min^{-1} under inert environment. All thermal graphs can be seen in Fig. S9–S11.†

Thicknesses of the materials were determined using a Mitutoyo micrometer. Membranes were measured at five different locations. Since the PI-IL composite membranes were tacky, to determine the thickness, the difference was taken between the film and PES support were measured, and then the known thickness of the Supor® was subtracted. An average of their differences of the membrane-PES and PES was used for the thickness variable within the permeation calculations. The thickness of the film was also observed using SEM to ensure the accuracy of the micrometer.

2.7 Gas permeability measurements

Gas permeation behavior of the ionene composite membranes were analyzed using pure gases (H_2, CO_2, N_2, and CH_4) to determine their permeability (P, in barrer), with the assumption that the mechanism of transport is solution–diffusion (S–D). P is taken to be the product of solubility (S) and diffusivity (D). The high vacuum time-lag systems are based on a constant-volume/variable-pressure method and used in this research, as described in previous works from our group,[16] and throughout the polymer gas separation membrane literature. A 47 mm diameter composite membrane is placed into a Millipore membrane holder with an O-ring. After the feed and permeate are held at dynamic vacuum for 24 h, pure gas is applied to ~3 atm (~44 psia) on the feed while the downstream pressure is at vacuum (~0.01 psia). According to the S–D model, the gas permeates through the dense film while the pressure of the downstream is recorded. The pure gas permeations are determined by calculating the linear steady-state increase of the permeate pressure against time (dp/dt). The time lag (θ) is used in part to determine the diffusivity of gas through the membrane. The ideal selectivities (α_{ij}) are determined as the quotient of the measured P (in barrer) of the individual gases of interest.

3. Results and discussion

To contextualize the experimental characterization and gas permeation results, computational studies focused on the impacts of C(2)-methylation were conducted to better understand the properties and performance trends for these materials.

3.1 Simulation outcomes

3.1.1 QM calculations. All QM calculations were performed with the ORCA[31,32] program by using the B97-3c functional.[33] This level of theory is generally applicable for estimating the chemical properties of large systems (here, 50–80 atoms) at a low-cost. Frequency calculations at the same level of theory were performed to confirm that all the structures correspond to minima on the potential energy surface. The partial charges of atoms in the charge-neutral molecules were calculated using both the ChelpG[34] method and CM5[35] at the same level using the Multiwfn program.[36] The optimized structures were visualized in GaussView[37] *via* OfakeG,[38] which converts ORCA output files to a Gaussian-like format. The chemical structures, optimized structures, and corresponding atomic charges are shown in Fig. 8 and 9, Fig. S14, and Table S1,† respectively.

In order to further investigate the structure–property relationships of these molecules, especially how the C(2)–Me group changes the electronic properties around the imidazolium cation, the electrostatic potential (ESP) and the reduced density gradient (RDG)[39] of these molecules were analyzed by Multiwfn and visualized by VMD.[40] The general interaction property functions (GIPF)[41] of these species were also generated to analyze the molecular electrostatic properties. The

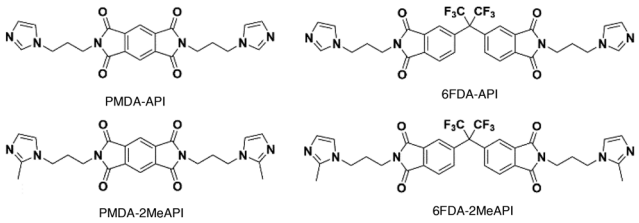

Fig. 8 Names and structures of monomers studied with QM.

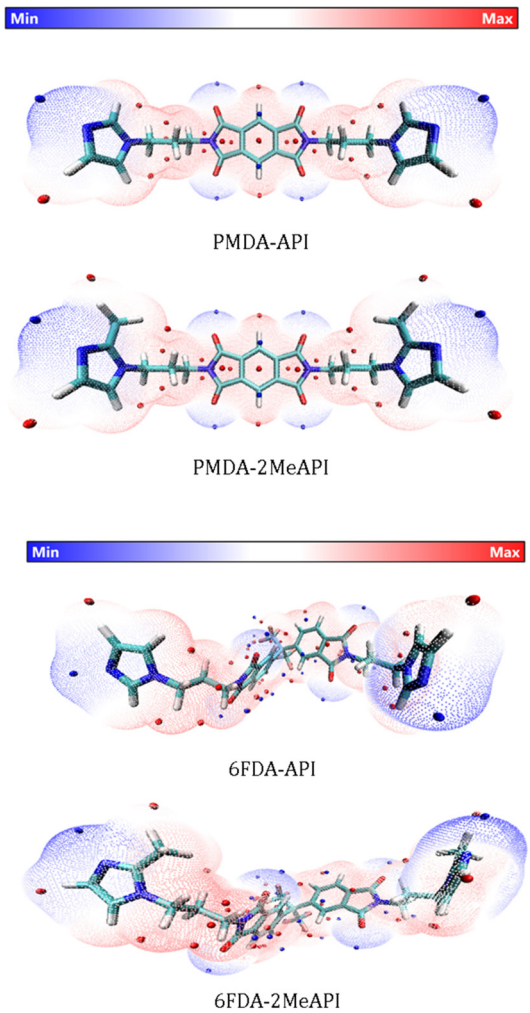

Fig. 9 ESP-mapped molecular vdW surfaces of the neutral monomers, corresponding to the ρ = 0.001 e/Bohr^3 isosurface. The color scale bar is shown at the top, while the corresponding ESP values (units of kcal mol^{-1}) are −50–50 kcal mol^{-1}. The local minima and maxima points on the ESP surface are represented as blue and red spheres, respectively. These species are represented as licorice models (cyan: C, white: H, red: O, blue: N, and pink: F).

GIPFs are derived from the molecular surface electrostatic potentials by mapping the electrostatic potential surface according to the van der Waals surfaces, as defined by Bader[42] (with the electron density isosurface corresponding to 0.001 e/Bohr^3).

3.1.2 QM results. The calculated atomic charges using the ChelpG and CM5 methods are listed in Table S1.† The charges on the C(2) positions increase after methylation, both for PMDA-API (C24 and C25) and 6FDA-API (C35 and C36). Using the ChelpG method, the charges dramatically increase from ~0.14 e to 0.46 e, while for the CM5 method, the charges slightly increase from ~0.13 e to 0.21 e. The discrepancies are mainly due to the inherent differences of the two calculation methods. For these larger species, the ChelpG method (derived from the electrostatic potential) can suffer from erroneous issues related to "buried atoms", while the CM5 partial atomic charges display more consistent behavior.[35] Furthermore, the C(2) positions in imidazole rings have the most positive charges, while C(4) and C(5) positions have lesser positive charges (0.14–0.15 e lower than C(2) positions) in both PMDA-API and 6FDA-API. Thus, based on the charges calculated using the CM5 method, the methylation on the C(2) positions of the imidazolium rings slightly increases their atomic charges (0.08 e). Besides, the C(2) positions in the molecules without methylation show higher positive charges than at the C(4) and C(5) positions, potentially explaining why the methylation at the C(2) positions are more significant than at either the C(4) or C(5) positions.

The ESP surface is mapped to the molecular vdW surface of these four species, as shown in Fig. 9, and the corresponding ESP distributions and GIPF descriptors are shown in Fig. S15 and Table S2,† respectively. From the ESP distributions of these molecules, the methylation for both PMDA-API and 6FDA-API make the ESP curves less positive. For the neutral species, the sites possessing more positive values (*i.e.*, the red spheres distributed on the red surface) have a stronger tendency to attract electrons and thus, are most likely the interaction sites with either the anions or the O atoms of CO_2. However, from the ESP surfaces, the methylation on the C(2) positions of both PMDA-API and 6FDA-API slightly weakens the ESP values around the C(2) atoms, which potentially decreases the electrostatic intermolecular interactions between these corresponding cationic species in the polymer chains with the anions.

Furthermore, the RDG analyses based on our DFT calculations are shown in Fig. 10. The RDG images, which help visualize the intramolecular non-covalent interactions, show weaker interactions between the methyl groups with the $-CH_2$ on the backbones of both PMDA-2MeAPI and 6FDA-2MeAPI, while these weaker interactions are not presented in either PMDA-API or 6FDA-API molecules. The RDG results indicate that the methylation on the C(2) positions slightly increase the intramolecular interactions between the imidazolium rings with the polymer chains in these molecules.

3.1.3 MD simulations. To further investigate the effects of methylation on the C(2) position of the imidazolium rings, simulations of the PI-ionenes were performed. Because of the structural flexibility of these molecules, there are many stable low-lying conformers that can be found. Thus, we performed MD simulations of the corresponding poly-ionic monomers, in order to sample the structural dynamics. These simulations

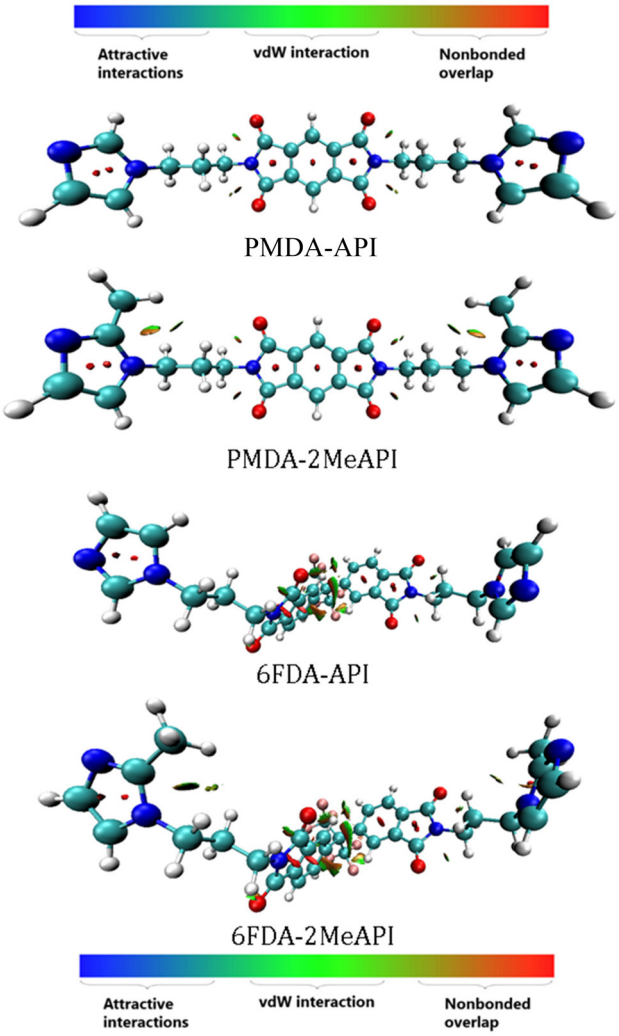

Fig. 10 Color-filled RDG map of the neutral monomers (isovalue of the RDG is set to 0.5). The value of sign(λ_2)$\rho(r)$ on the surfaces is represented by the color bar at top, where sign(λ_2) is the sign of the second largest eigenvalue of the Hessian of $\rho(r)$. The surfaces are colored on a blue-green-red scale according to values of sign(λ_2)$\rho(r)$, ranging from −0.04 to 0.02 au. Blue indicates strong attractive interactions, and red indicates strong nonbonded overlap. The species are represented as CPK models (cyan: C, white: H, red: O, blue: N, and pink: F).

included one positively charged polymer chain segment (PMDA-API, PMDA-2MeAPI, 6FDA-API and 6FDA-2MeAPI with benzyl groups ($-CH_2-C_6H_6$) at both termini) with two negatively charged anions ($[Tf_2N]^-$). Although the monomer structures during the MD simulations do not truly emulate the liquid state environment, the main types of anion–cation interactions can still be captured adequately, which helps us theoretically quantify the effect of the C(2) methylation. The MD simulations were performed with the newly-developed GFN-FF[43] using xTb.[44] This approach has been found to yield results nearing the accuracy of semi-empirical QM methods, and in some cases reaching even DFT accuracy.[43]

In order to perform the MD simulations, the optimized geometries of the ionic molecules and anions were inserted into

the simulation boxes at close distances (~5 Å), followed by a few pre-optimization steps to adjust the covalent-bonding network. Then, NVT ensemble simulations (constant volume and temperature) were performed at 300 K using a total of 250 ps for equilibrium, followed by another 250 ps for production (time step of 1 fs). The simulations were accelerated by constraining the X–H bonds in the system. A total of 10^4 trajectories were used to generate the spatial distribution function (SDF) and connection matrix (CMat) using the Travis package.[45,46]

For reference, the initial and final snapshots of these systems are shown in Fig. S16.† The initial molecular geometries optimized using DFT calculations are almost linear structures, while after the MD simulations, the polymer chains tend to fold together. In order to gain a deeper insight into the intermolecular and intramolecular interactions within these polymer chains, the SDFs are shown in Fig. 11, and the CMats of all non-carbon atoms in the cationic molecules with the anions and the CMats for the intramolecular interactions within the positively-charged species are shown in Fig. S17 and S18,† respectively. In Fig. 11, the anionic species are located around the O atom sites of the backbones and near the H atoms of the imidazolium rings in both PMDA-API and PMDA-2MeAPI. While for both 6FDA-API and 6FDA-2MeAPI, the anionic species are located around the O and F atom sites of the backbones and near the H atoms of the imidazolium ring (of 6FDA-API) and near the O atoms and the ring-bound H atoms (of 6FDA-2MeAPI).

The CMats for these monomers show the potential binding sites between the cationic species with the anions. Here, we focus on the changes of intermolecular H-bonding between the counterions and the intramolecular H-bonding within cationic polymer chains before and after C(2) methylation. We focus on the interactions between the H atoms in PMDA-API (H49 and H50) and 6FDA-API (H68 and H69) and the H atoms in the $-CH_3$ groups in PMDA-2MeAPI (H52–54 and H56–58) and 6FDA-2MeAPI (H71–73 and H75–77) with the H-bond acceptors. The slightly stronger H-bonding *via* the O atom sites, and the weaker H-bonding *via* the F atom sites of the anions highlight the increased H-bonding interaction after methylation of both PMDA-API and 6FDA-API. Examples of potential H-bonding networks between the $-CH_3$ groups in PMDA-2MeAPI and 6FDA-2MeAPI with the O atom sites in the $[Tf_2N]^-$ anions during MD simulations are shown in Fig. 12. Due to thermal fluctuations, the binding sites and bond distances change during the MD simulations. Although the true liquid state is not captured, the main types of anion–cation interactions should still be consistent. Thus, based on the CMat analyses from the MD simulations, the methylation of C(2) positions on the imidazolium ring potentially increases the chance of H-bonding between the cationic species with the anions by providing more binding sites *via* $-CH_3$. Furthermore, the SDFs show that the methylation of the C(2) positions slightly decreases the intramolecular interactions *via* electrostatic interaction, while increasing the hydrogen bonding interactions by providing more H sites in $-CH_3$ (confirmed by the CMat intramolecular H-bonding analyses in Fig. S18†).

In conclusion, the intermolecular SDF results show that the methylation at the C(2) position of the imidazolium rings decreases the intermolecular interactions (mainly *via* electrostatic interactions) between the positively-charged polymer chain with the $[Tf_2N]^-$ anions, while slightly increasing the intramolecular H-bonding interaction within positively-charged polymer chains. This is corroborated with the inter- and intra-molecular CMat analyses, along with the ESP and RDG analyses based on DFT calculations.

3.2 Material characterization

Glass transition temperatures (T_g) were determined from the DSC thermograms. The T_g values were less than their counterparts from a previous work.[47] The changes in T_g can be attributed to the reduction of H-bonding within the supramolecular polymer structure of both polymers. While both ionenes contain diimides, it should be noted that the PMDA segment is essentially planar while 6FDA is non-planar (due to the CF_3 group repulsions) and known to introduce a kink along polyimide chains. Additionally, larger delocalized anions like $[Tf_2N^-]$ are known to decrease the T_g in corresponding cationic polymers, due to weakened electrostatic interactions with the

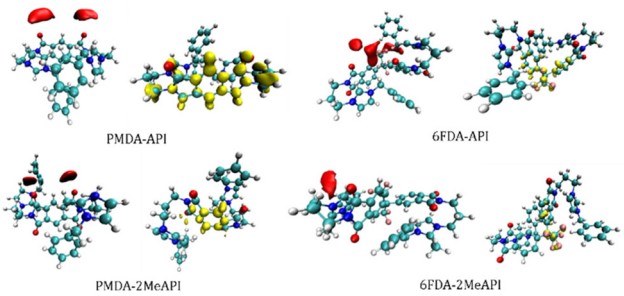

Fig. 11 The SDFs of anions (red) and cationic polymer chains (gold) around the positively charged polymer chain. The corresponding isovalues for the anion and cationic species of number densities are 10 nm^{-3} and 4 nm^{-3}, respectively. The central positively charged polymer chain are represented as CPK models.

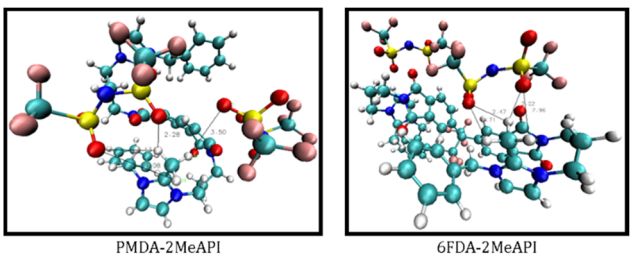

Fig. 12 Examples of potential H-bonding networks between the $-CH_3$ groups in PMDA-2MeAPI and 6FDA-2MeAPI with the O atoms in the $[Tf_2N]^-$ anions during the MD simulations. Binding sites and bond distances (listed in the text with units of Å) vary during the MD simulations.

associated cation. Further, [Tf_2N^-] corresponds to a significant portion of the total polymer mass (41–50 wt%), and this anion bulk has been shown to notably influence the mobility of the corresponding cationic chains. Comparing [PMDA-API(pXy)][Tf_2N] and [PMDA-2MeAPI(pXy)][Tf_2N], the reduction in T_g was from 106.8 °C to 87.0 °C, which according to the computational results may be attributed to the further decreased electrostatic interactions between the anion and cationic backbone from methylation of the C(2) position. Due to the presence of a semi-crystalline peak in the XRD profiles (Fig. 13), [PMDA-API(pXy)][Tf_2N] neat or with IL, is slightly more regularly ordered and may entangle and/or align more efficiently, due to the stronger interactions which affect chain mobility, when compared to [PMDA-2MeAPI(pXy)][Tf_2N]. These stacking interactions and the planarity of the PMDA-based diimide segment appears to be disrupted by the C(2)–Me presence and corresponding suppression in cation–anion associations.

However, the T_g values of [6FDA-API(pXy)][Tf_2N] and [6FDA-2MeAPI(pXy)][Tf_2N] were observed to increase from 93.5 °C to 107.4 °C, respectively. Due to the bent nature of 6FDA the contortion and conformation which dictate chain entanglement may be more significantly affected by the increased intramolecular H-bonding and decreased electrostatic interactions. The interchain interactions may be amplified for the C(2)–Me derivative, relative to the more irregular stacking interactions, due to the inherent kinks and increased distance between the anion and cationic backbone.

WAXD was used to approximate the domain spacings of the polymer films, as well as to elucidate the effects of the IL on the chain–chain spacing, coordinating effects, and molecular interactions. Due to their random nature, amorphous polymers produced a broad halo, corresponding to a range of chain–chain spacings of a polymer. [PMDA-2MeAPI(pXy)][Tf_2N] and [6FDA-2MeAPI(pXy)][Tf_2N] produced profiles with 2θ = 19.5–22.5° and 2θ = 18.3–20.5°, respectively whereas their counterparts, [PMDA-API(pXy)][Tf_2N] and [6FDA-API(pXy)][Tf_2N], show halos from 2θ = 20–24° and 2θ = 17.5–22.0° (Fig. 13 and 14). The *d*-spacing ranges are reported in Table 1 along with the estimated mean or most intense "peak" value noted. With the presence of a C(2)–Me group on the imidazolium cation, the 2θ distribution slightly shifted, corresponding to increased *d*-spacings. This is in agreement with the simulated decrease in electrostatic interactions observed for the C(2)-methylated derivatives. In [PMDA-2MeAPI(pXy)][Tf_2N], the semicrystalline peak is diminished, indicating the C(2)–H played a vital role in the regularity and strength of intermolecular forces present between anion–cation pairs, and by extension other stacking interactions may have been disrupted. Regardless, these *d*-spacing ranges correlated well to the range of interchain spacings reported for other polyimides (~ 5.5 Å).[48]

The addition of IL was shown to broaden the main halo for all derivatives, and thus decreases the regularity and uniformity of interchain spacings amongst ionene chains. Addition of [C_4mim][Tf_2N] decreased the *d*-spacing range as well. This is attributed to the voids filled by IL, as well as the increase in electrostatic and H-bonding participants within these composite systems, yet the decrease is not substantial. The n-butyl group of the [C_4mim][Tf_2N] may also hinder interactions

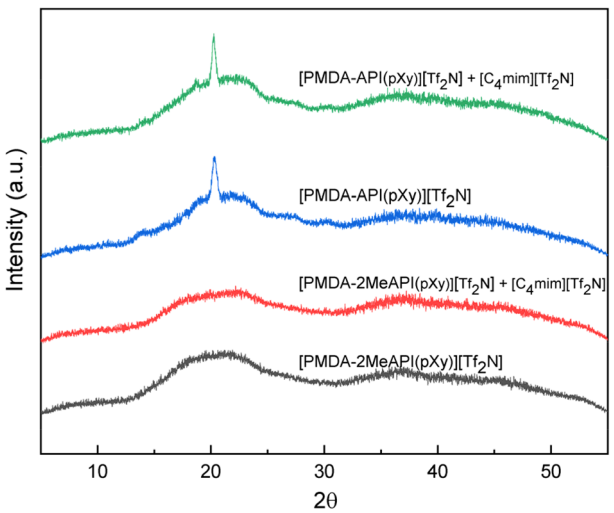

Fig. 13 XRD profiles of PMDA C(2)–H and C(2)–Me, both neat and composite PI-ionenes.

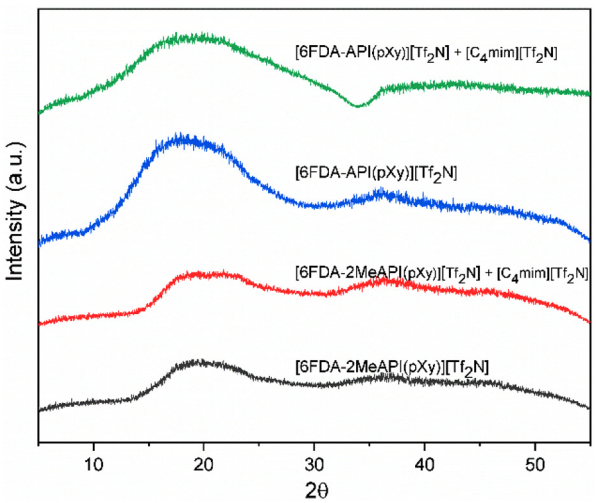

Fig. 14 XRD profiles of 6FDA C(2)–H and C(2)–Me, both neat and composite, PIs.

Table 1 Halo and peak values of neat and IL composites of C(2)–Me materials and C(2)–H materials

	Neat	Composite	Neat	Composite
	[PMDA-2MeAPI (pXy)][Tf_2N]		**[6FDA-2MeAPI (pXy)][Tf_2N]**	
Halo (Å)	4.77–5.72	4.56–5.72	5.03–5.81	4.51–5.81
Peak (Å)	4.77	4.56	5.15	4.75
	[PMDA-API(pXy)][Tf_2N]		**[6FDA-API(pXy)][Tf_2N]**	
Halo (Å)	4.54–5.36	4.45–5.48	5.10–6.16	4.93–6.23
Peak (Å)	5.05	5.07	5.65	5.15

between charged segments or impede the packing, causing only a slight reduction of 2θ range within both [PMDA-2MeAPI(pXy)][Tf_2N] and [6FDA-2MeAPI(pXy)][Tf_2N] + IL composites.

FT-IR measurements were performed on all materials to validate the structural composition/functional groups along verifying the presence of IL within the polymer matrix. The spectra are provided in Fig. S7.† FT-IR spectra were normalized to the carbonyl stretching (C═O) peak at 1720 cm^{-1}. The formation of the imide ring and imidazolium can be found in the C–N–C out-of-plane bending and stretching at 721 cm^{-1} and 1100 cm^{-1}, respectively. The sulfonyl (S═O) stretching within a sulfonimide at peaks 1370–1335 cm^{-1} and the S–N–S stretching at 760 cm^{-1} indicate complete exchange of Cl^- to $[Tf_2N]^-$ in the final PI-ionenes. The increase of the S═O and S–N–S stretching were denoted in the composite membranes to demonstrate the incorporation [C_4mim][Tf_2N] into the polymer matrix.

3.3 Gas separation performances of PI-ionene + IL composite membranes

The permeabilities, diffusivities, and solubilities are summarized in Table 2. Both the [PMDA-2MeAPI(pXy)][Tf_2N] + [C_4mim][Tf_2N] and [6FDA-2MeAPI(pXy)][Tf_2N] + [C_4mim][Tf_2N] showed moderate gas separation ability for all gases (N_2, CH_4, CO_2, and H_2) where both C(2)–Me composites decreased when compared to their direct counterpart with C(2)–H groups. Comparing the [PMDA-API(pXy)][Tf_2N] + [C_4mim][Tf_2N] and [PMDA-2MeAPI(pXy)][Tf_2N] + [C_4mim][Tf_2N], the addition of the methyl group caused significant decreases in all gas diffusivities by factors over 10×, while slight increases in solubility were observed. As seen in research related to ILs with C(2)–Me imidazolium cations, the CO_2 solubility did not change with the addition of a methyl group on the acidic C(2) position. The gas solubility of similar ILs was determined to be directly related to the anion affinity for CO_2 within the IL.[48]

The structural influence on permeabilities of both [PMDA-2MeAPI(pXy)][Tf_2N] + [C_4mim][Tf_2N] and [6FDA-2MeAPI(pXy)][Tf_2N] + [C_4mim][Tf_2N] can be compared, since these differ with respect to the linearity and planarity of the dianhydride precursor. Koros and co-workers compared PMDA and 6FDA in two instances, and the increase in the permeability for the more contorted 6FDA analogues are consistent.[50,51] In both cases, the addition of a methyl group at the imidazolium C(2) was shown to decrease P_{CO_2}, although comparable selectivities when compared to the C(2)–H derivatives were maintained. In this instance, C(2)-methylation further supports that 6FDA-based ionic polyimides may be superior to PMDA derivatives, when looking to improve gas permeabilities by increasing FFV. Yet, with respect to the ionic polymer architecture and regularity of chain ordering, the C(2) position can be seen as an integral influence on these polymer composites. When comparing the permeabilities of the IL composites with and without a methyl group, the non-methylated counterparts have higher permeabilities with respect to all gases tested than either [PMDA-2MeAPI(pXy)][Tf_2N] + [C_4mim][Tf_2N] or [6FDA-2MeAPI(pXy)][Tf_2N] + [C_4mim][Tf_2N]. As an indicator of permeability, the *d*-spacing relationships can be a correlative factor since these are related to chain–chain spacings within a polymer matrix. This phenomenon is also demonstrated here, as the derivatives with decreased *d*-spacing distributions exhibited diminished permeabilities. It should also be noted that the method of IL impregnation may influence this, as the C(2)–H PMDA derivative was allowed to soak in [C_4mim][Tf_2N], whereas these composites were prepared from solution casting. Additionally, the effects of C(2)–Me for the 6FDA analogues were minor, only resulting in small permeability decreases (12–25%) for CO_2, CH_4, and N_2, which may signify that other structural features dominate chain organization in these systems. Although other factors contribute to the gas separation ability, the permeabilities and *d*-spacing range were higher for [6FDA-2MeAPI(pXy)][Tf_2N] + [C_4mim][Tf_2N] than [PMDA-2MeAPI(pXy)][Tf_2N] + [C_4mim][Tf_2N]. Thus, the correlation between *d*-spacing and permeability holds true for these membranes, as seen for other similar ionic polymer systems.[17,18,52,53] It should be noted that H_2 permeabilities were still lower than CO_2 when IL was present in the polymer matrix, as the permselectivity of CO_2/H_2 is >1.

The QM calculations and MD simulations validate these gas permeation results and the changes within the *d*-spacings. The MD simulations indicate that many conformations exist for these molecules, and thus a broad range of interchain spacings would be expected for these amorphous composites. As stated in the discussion of QM simulations, both 6FDA-2MeAPI and PMDA-2MeAPI molecules exhibited altered charges, potentially demonstrating increased interactions between the C(2)-position and the O atoms in Tf_2N or CO_2. However, the MD simulations indicate increased intramolecular interactions between polymer chains due to the increased H-bonding sites, which may cause the observed decrease in permeability when comparing the API and 2MeAPI derivatives. Factors like the increase in H-bonding between the cationic chains and introduction of free IL may supersede the modified electrostatic interactions from C(2)-methylation. The effects further are supported in the XRD results, as well as the

Table 2 Permeability values[a,b] of [PMDA-2MeAPI(pXy)][Tf_2N] + [C_4mim][Tf_2N] and [6FDA-2MeAPI(pXy)][Tf_2N] + [C_4mim][Tf_2N] IL and comparisons to previously published values

	[PMDA-2MeAPI(pXy)][Tf_2N] + IL	[6FDA-2MeAPI(pXy)][Tf_2N] + IL
N_2	0.07 ± 0.01	0.16 ± 0.01
CH_4	0.08 ± 0.01	0.16 ± 0.02
H_2	1.34 ± 0.02	3.89 ± 0.05
CO_2	2.75 ± 0.03	5.75 ± 0.03
	[PMDA-API(pXy)][Tf_2N] + IL	**[6FDA-API(pXy)][Tf_2N] + IL**
N_2	0.52 ± 0.02	0.20 ± 0.03
CH_4	0.79 ± 0.02	0.18 ± 0.02
H_2	5.18 ± 0.04	3.59 ± 0.25
CO_2	20.4 ± 0.1	6.58 ± 0.15

[a] Three replicate experiments were performed, and thus uncertainties are presented as a single standard deviation. [b] Permeability in barrer (10^{-10} (cm^3 (STP) cm) (cm^2 s cmHg)$^{-1}$). – *P* data for [6FDA-2MeAPI(pXy)][Tf_2N] + [C_4mim][Tf_2N] from O'Harra *et al.*[49]

Table 3 Permeability selectivities for selected gas pairs for membranes synthesized in this work

Pair	[PMDA-2MeAPI(pXy)][Tf_2N] + IL	[6FDA-2MeAPI(pXy)][Tf_2N] + IL
CO_2/N_2	41.0	35.4
CO_2/CH_4	33.1	35.5
H_2/N_2	20.0	24.7
H_2/CH_4	16.1	24.8
CO_2/H_2	2.05	1.43

gas permeation data, which these simulations prove that the addition of the $-CH_3$ on the C(2) position has substantial influence over the neat materials, but is not a determinant effect on the structuring and performance of these IL-composite systems.

Selectivity values were also calculated from permeabilities, s reported in Table 3. Based on our prior work with ionenes and ILs, CO_2 selectivity is driven by solubility (*e.g.*, condensability, quadrupole) whereas H_2 selectivity is favored by diffusion (*i.e.*, smallest gas)[54] Permselectivities of the IL-composite membranes coincided with the inverse relationship of permeability/selectivity. The relationship is demonstrated by Robeson's Upper Bound when plotting CO_2 permeability *versus* CO_2 selectivity.[55,56] Robeson plots with similar ionic gas separation membranes are provided as Fig. S19 and S20.† The materials were below the upper bound and within the bulk of other materials when comparing CO_2/N_2 and CO_2/CH_4 separations.

4. Conclusions

This study computationally and experimentally explored the effects of C(2)-methylation of the imidazole ring in high-performance, imidazolium ionenes. This work reports the synthesis and modeling of two new polyimide ionenes for comparison with previous analogues, one of few examples of imidazolium ionenes with substitution rather than a proton at the acidic C(2) site. 2MeAPI was reacted with two common dianhydrides (planar PMDA and bent 6FDA) through a condensation reaction to form two new bis(imidazole) diimide monomers. These monomers were then polymerized *via* the Menshutkin reaction, followed by anion metathesis to exchange the halide with [Tf_2N^-]. The materials were characterized *via* NMR and FT-IR to ensure the structure of the material, and the thermal properties of [PMDA-2MeAPI(pXy)][Tf_2N] and [6FDA-2MeAPI (pXy)][Tf_2N] were also measured. The XRD profiles demonstrated that the C(2)–Me ionenes experienced a significant decrease in the regularity of chain packing and morphology of these materials. The glassy neat materials were impregnated with a stoichiometric equivalent of IL, which resulted in amorphous composites with increased membrane flexibility, altered chain ordering/structure, and increased P_{CO_2}. The gas transport behaviors were tested for two polyimide ionene composites with [C_4mim][Tf_2N], which demonstrated that the C(2)-methylation and IL caused the diffusivity to significantly decrease while slightly increasing the solubility. These materials exhibited lowered gas permeabilities than their C(2)–H counterparts, which was supported by computational insights, indicative of increased intrachain interactions due to additional H-bonding sites along these cationic ionenes and decreased intermolecular and electrostatic interactions between the positively-charged backbone and paired anions or CO_2. Due to the ionic nature of the films, it was still observed that these membranes have an affinity for polar *vs.* non-polar gases and maintained distinct CO_2 selectivities, particularly against N_2 and CH_4. The correlations between the QM and MD simulations and the structural changes and performance of these materials as gas separation membranes were summarized.

Author contributions

Manuscript preparation (GPD, KEO, JEB), writing (GPD), manuscript revision and editing (GPD, KEO), material synthesis (KEO), material characterizations (KEO, EMJ), gas permeation studies (GPD), funding acquisition and project management (JEB, CHT), computational studies and analysis (XL, CHT). All authors contributed to this manuscript and approved its final form.

Conflicts of interest

There are no conflicts to declare.

Acknowledgements

JEB and CHT acknowledge support from the U.S. National Science Foundation (CBET-1605411). JEB and EMJ acknowledge support from NASA Marshall Space Flight Center (80MSFC19M0048). KEO acknowledges a GAANN Fellowship from the United States Department of Education (P200A180056).

References

1 K. C. O'Brien, W. J. Koros and G. R. Husk, *Polym. Eng. Sci.*, 1987, **27**, 211–217.
2 Y. Hirayama, T. Yoshinaga, Y. Kusuki, K. Ninomiya, T. Sakakibara and T. Tamari, *J. Membr. Sci.*, 1996, **111**, 169–182.
3 S. A. Stern, Y. Liu and W. A. Feld, *J. Polym. Sci., Part B: Polym. Phys.*, 1993, **31**, 939–951.
4 S. R. Williams and T. E. Long, *Prog. Polym. Sci.*, 2009, **34**, 762–782.
5 E. B. Anderson and T. E. Long, *Polymer*, 2010, **51**, 2447–2454.
6 K. E. O'Harra and J. E. Bara, *Polym. Int.*, 2021, **70**, 944–950.
7 J. E. Bara and K. E. O'Harra, *Macromol. Chem. Phys.*, 2019, **220**, 1900078.

8 J. S. Lee, A. Hocken and M. D. Green, *Mol. Syst. Des. Eng.*, 2021, **6**, 334–354.
9 C. F. Gibbs, E. R. Littmann and C. S. Marvel, *J. Am. Chem. Soc.*, 1933, **55**, 753–757.
10 M. T. Bogert, *Science*, 1933, **77**, 197–198.
11 P. Scovazzo, J. Kieft, D. A. Finan, C. Koval, D. DuBois and R. Noble, *J. Membr. Sci.*, 2004, **238**, 57–63.
12 K. Friess, P. Izák, M. Kárászová, M. Pasichnyk, M. Lanč, D. Nikolaeva, P. Luis and J. C. Jansen, *Membranes*, 2021, **11**, 97.
13 P. Li, Q. Zhao, J. L. Anderson, S. Varanasi and M. R. Coleman, *J. Polym. Sci., Part A: Polym. Chem.*, 2010, **48**, 4036–4046.
14 C. Zhang, B. Cao, M. R. Coleman and P. Li, *J. Appl. Polym. Sci.*, 2016, **133**, 43077.
15 P. Li and M. R. Coleman, *Eur. Polym. J.*, 2013, **49**, 482–491.
16 M. S. Mittenthal, B. S. Flowers, J. E. Bara, J. W. Whitley, S. K. Spear, J. D. Roveda, D. A. Wallace, M. S. Shannon, R. Holler, R. Martens and D. T. Daly, *Ind. Eng. Chem. Res.*, 2017, **56**, 5055–5069.
17 K. E. O'Harra, I. Kammakakam, D. M. Noll, E. M. Turflinger, G. P. Dennis, E. M. Jackson and J. E. Bara, *Membranes*, 2020, **10**, 51.
18 K. E. O'Harra, I. Kammakakam, E. M. Devriese, D. M. Noll, J. E. Bara and E. M. Jackson, *Membranes*, 2019, **9**, 79.
19 P. Bonhôte, A.-P. Dias, N. Papageorgiou, K. Kalyanasundaram and M. Grätzel, *Inorg. Chem.*, 1996, **35**, 1168–1178.
20 P. A. Hunt, *J. Phys. Chem. B*, 2007, **111**, 4844–4853.
21 T. Endo, T. Kato and K. Nishikawa, *J. Phys. Chem. B*, 2010, **114**, 9201–9208.
22 K. Fumino, A. Wulf and R. Ludwig, *Angew. Chem., Int. Ed.*, 2008, **47**, 8731–8734.
23 K. Noack, P. S. Schulz, N. Paape, J. Kiefer, P. Wasserscheid and A. Leipertz, *Phys. Chem. Chem. Phys.*, 2010, **12**, 14153–14161.
24 S. Zahn, G. Bruns, J. Thar and B. Kirchner, *Phys. Chem. Chem. Phys.*, 2008, **10**, 6921–6924.
25 B. Lin, H. Dong, Y. Li, Z. Si, F. Gu and F. Yan, *Chem. Mater.*, 2013, **25**, 1858–1867.
26 K. Fumino, T. Peppel, M. Geppert-Rybczynska, D. H. Zaitsau, J. K. Lehmann, S. P. Verevkin, M. Kockerling and R. Ludwig, *Phys. Chem. Chem. Phys.*, 2011, **13**, 14064–14075.
27 T. K. Carlisle, J. E. Bara, A. L. Lafrate, D. L. Gin and R. D. Noble, *J. Membr. Sci.*, 2010, **359**, 37–43.
28 X. He and T. H. Chan, *Org. Lett.*, 2007, **9**, 2681–2684.
29 J. Demarteau, K. E. O'Harra, J. E. Bara and H. Sardon, *ChemSusChem*, 2020, **13**, 3122–3126.
30 T. J. Schwan, *J. Heterocycl. Chem.*, 1967, **4**, 633–634.
31 F. Neese, *Wiley Interdiscip. Rev.: Comput. Mol. Sci.*, 2012, **2**, 73–78.
32 F. Neese, *Wiley Interdiscip. Rev.: Comput. Mol. Sci.*, 2018, **8**, e1327.
33 J. G. Brandenburg, C. Bannwarth, A. Hansen and S. Grimme, *J. Chem. Phys.*, 2018, **148**, 064104.
34 C. M. Breneman and K. B. Wiberg, *J. Comput. Chem.*, 1990, **11**, 361–373.
35 A. V. Marenich, S. V. Jerome, C. J. Cramer and D. G. Truhlar, *J. Chem. Theory Comput.*, 2012, **8**, 527–541.
36 T. Lu and F. Chen, *J. Comput. Chem.*, 2012, **33**, 580–592.
37 R. Dennington, T. Keith and J. Millam, *GaussView*, Version 5, 2009.
38 T. Lu, *OfakeG program*, Version 1.0.6, **http://sobereva.com/soft/OfakeG**, (accessed May, 2020).
39 E. R. Johnson, S. Keinan, P. Mori-Sánchez, J. Contreras-García, A. J. Cohen and W. Yang, *J. Am. Chem. Soc.*, 2010, **132**, 6498–6506.
40 W. Humphrey, A. Dalke and K. Schulten, *J. Mol. Graphics*, 1996, **14**, 33–38.
41 J. S. Murray, T. Brinck, P. Lane, K. Paulsen and P. Politzer, *J. Mol. Struct.: THEOCHEM*, 1994, **307**, 55–64.
42 R. F. Bader, M. T. Carroll, J. R. Cheeseman and C. Chang, *J. Am. Chem. Soc.*, 1987, **109**, 7968–7979.
43 S. Spicher and S. Grimme, *Angew. Chem., Int. Ed.*, 2020, **59**, 15665–15673.
44 S. Grimme, C. Bannwarth and P. Shushkov, *J. Chem. Theory Comput.*, 2017, **13**, 1989–2009.
45 B. Martin and B. Kirchner, *J. Chem. Inf. Model.*, 2011, **51**, 2007–2023.
46 M. Brehm, M. Thomas, S. Gehrke and B. Kirchner, *J. Chem. Phys.*, 2020, **152**, 164105.
47 K. E. O'Harra, I. Kammakakam, J. E. Bara and E. M. Jackson, *Polym. Int.*, 2019, **68**, 1547–1556.
48 A. Shimazu, T. Miyazaki and K. Ikeda, *J. Membr. Sci.*, 2000, **166**, 113–118.
49 K. E. O'Harra, I. Kammakakam, E. M. Devriese, D. M. Noll, J. E. Bara and E. M. Jackson, *Membranes*, 2019, **9**, 79.
50 T. H. Kim, W. J. Koros and G. R. Husk, *Sep. Sci. Technol.*, 1988, **23**, 1611–1626.
51 T. H. Kim, W. J. Koros, G. R. Husk and K. C. O'Brien, *J. Membr. Sci.*, 1988, **37**, 45–62.
52 I. Kammakakam, K. E. Oharra, J. E. Bara and E. M. Jackson, *ACS Omega*, 2019, **4**, 3439–3448.
53 I. Kammakakam, K. E. O'Harra, G. P. Dennis, E. M. Jackson and J. E. Bara, *Polym. Int.*, 2019, **68**, 1123–1129.
54 M. S. Mittenthal, B. S. Flowers, J. E. Bara, J. W. Whitley, S. K. Spear, J. D. Roveda, D. A. Wallace, M. S. Shannon, R. Holler, R. Martens and D. T. Daly, *Ind. Eng. Chem. Res.*, 2017, **56**, 5055–5069.
55 L. M. Robeson, *J. Membr. Sci.*, 1991, **62**, 165–185.
56 L. M. Robeson, *J. Membr. Sci.*, 2008, **320**, 390–400.